HHS Public Access

Author manuscript

Nat Med. Author manuscript; available in PMC 2019 January 01.

Published in final edited form as:

Nat Med. 2018 January ; 24(1): 29–38. doi:10.1038/nm.4443.

Amyloid-β plaques enhance Alzheimer's brain tau-seeded pathologies by facilitating neuritic plaque tau aggregation

Zhuohao He[1], **Jing L Guo**[1], **Jennifer D McBride**[1], **Sneha Narasimhan**[1], **Hyesung Kim**[1], **Lakshmi Changolkar**[1], **Bin Zhang**[1], **Ronald J Gathagan**[1], **Cuiyong Yue**[2], **Christopher Dengler**[2], **Anna Stieber**[1], **Magdalena Nitla**[1], **Douglas A Coulter**[2,3], **Ted Abel**[4], **Kurt R Brunden**[1], **John Q Trojanowski**[1], and **Virginia M-Y Lee**[1]

[1]Department of Pathology and Laboratory Medicine, Institute on Aging and Center for Neurodegenerative Disease Research, University of Pennsylvania School of Medicine, Philadelphia, Pennsylvania, USA

[2]Division of Neurology, The Children's Hospital of Philadelphia, Philadelphia, Pennsylvania, USA

[3]Departments of Neuroscience and of Pediatrics, University of Pennsylvania School of Medicine, Philadelphia, Pennsylvania, USA

[4]Iowa Neuroscience Institute and Department of Molecular Physiology and Biophysics, Carver College of Medicine, University of Iowa, Iowa City, Iowa, USA

Abstract

Alzheimer's disease (AD) is characterized by extracellular amyloid-β (Aβ) plaques and intracellular tau inclusions. However, the exact mechanistic link between these two AD lesions remains enigmatic. Through injection of human AD-brain-derived pathological tau (AD-tau) into Aβ plaque–bearing mouse models that do not overexpress tau, we recapitulated the formation of three major types of AD-relevant tau pathologies: tau aggregates in dystrophic neurites surrounding Aβ plaques (NP tau), AD-like neurofibrillary tangles (NFTs) and neuropil threads (NTs). These distinct tau pathologies have different temporal onsets and functional consequences on neural activity and behavior. Notably, we found that Aβ plaques created a unique environment that facilitated the rapid amplification of proteopathic AD-tau seeds into large tau aggregates, initially appearing as NP tau, which was followed by the formation and spread of NFTs and NTs,

Correspondence should be addressed to V.M.-Y.L. (vmylee@upenn.edu).

Note: Any Supplementary Information and Source Data files are available in the online version of the paper.

AUTHOR CONTRIBUTIONS

Z.H. designed the studies with the help of J.L.G., generated most of the data along with J.D.M. and interpreted all the results. J.L.G. and L.C. purified brain lysates for injection. S.N. provided the data of AD-WT mice at 9 m.p.i., and H.K. did the manual quantification for NIs and NP tau. B.Z. and R.J.G. performed mouse brain injection surgeries, A.S. did the immuno-EM and M.N. bred 5xFAD mice. C.Y., C.D. and D.A.C. performed neural circuit recording. K.R.B. and J.Q.T. participated in discussion of results and design of some experiments, as well as in writing of the manuscript. T.A. participated in experimental design and interpreting behavior results. Z.H. and V.M.-Y.L. wrote the manuscript, and all coauthors read and approved the manuscript. V.M.-Y.L. supervised the study.

COMPETING FINANCIAL INTERESTS

The authors declare no competing financial interests.

likely through secondary seeding events. Our study provides insights into a new multistep mechanism underlying Aβ plaque–associated tau pathogenesis.

In the course of AD, the accumulation of Aβ plaques is considered an early event, whereas the formation of tau NFTs is thought to be the more proximal cause of later neuronal dysfunction and degeneration[1–3]. The distribution of NFTs is usually restricted to the medial temporal lobe at early Braak stages of AD pathology, whereas at later Braak stages tau pathology spreads outside the temporal lobe into Aβ-rich areas, such as limbic and association cortices, concomitantly with substantial cognitive dysfunction[4–9]. These findings lend support to the amyloid cascade hypothesis, which states that Aβ promotes NFT formation in AD[1]. However, this hypothesis has not been proven, and the underlying mechanisms are enigmatic. Previous studies have attempted to elucidate the interaction between Aβ plaques and NFTs using transgenic mice overexpressing human tau (encoded by *MAPT*) with or without the mutations found in rare cases of autosomal dominant frontotemporal degeneration (FTD)[10–16]. However, it is unclear whether these results are applicable to AD, as heterologous promoters were used to drive transgene overexpression and upregulation or mutation of tau has never been demonstrated in AD. Recently, we established a new paradigm through induction of tau pathologies in wild-type (WT) mice via intracerebral injection of AD-tau[17], which provides a unique opportunity to re-examine the amyloid cascade hypothesis in mice with endogenous levels of tau expression.

RESULTS

Aβ plaques facilitate AD-tau-induced NP tau formation in dystrophic axons rather than NFT tau formation in neuronal somas at early seeding stages

Following our recently established protocol[17], we extracted sarkosyl-insoluble human AD-tau from the frontal cortices of two sporadic AD brains with a similar histological Braak stage and obtained lysates from two age-matched control brains. To test whether Aβ accumulation promotes the propagation of NFTs in mice without tau overexpression, we unilaterally injected human AD-tau (2 μg/mouse) into the dorsal hippocampus and overlying cortex of ~15-month-old WT mice and mice with knock-in of the mutated *APP* gene encoding mutant Aβ precursor protein (APP-KI mice), which do not overexpress APP or presinilin-1 (PS1) but develop moderate Aβ plaques in both cortex and hippocampus after 15 months of age[18]. Henceforth, we indicate the age at which mice received AD-tau injections in parentheses. The overall abundance and distribution of AD-like NFTs (hereafter referred to as NFTs) were similar between AD-tau-injected APP-KI (AD-APP-KI) (15 months) mice and AD-tau-injected WT (AD-WT) (15 months) mice at 3 months post-injection (m.p.i.), as indicated by immunostaining with two monoclonal antibodies against phosphorylated tau, AT8 and AT180 (Fig. 1a,b,o, and Supplementary Fig. 1a–d). Surprisingly, AD-APP-KI (15 months) mice showed another type of tau pathology that resembled NP tau with clusters of AT8-stained ($AT8^+$) tau granules and neurites surrounding Aβ plaque cores (Fig. 1b,**m**); this was absent in 15-month-old APP-KI mice injected with similarly prepared brain extracts from age-matched control subjects (Fig. 1c). Furthermore, both NFTs and NP tau were also present in 15-month-old APP-KI mice injected with AD-tau purified from a different AD case (Supplementary Fig. 1f), revealing that the induction

of these two types of tau pathology is due to AD-tau and is not dependent on the AD case. Moreover, both types of tau pathology were labeled by a mouse-tau-specific antibody, R2295, but not a human-tau-specific monoclonal antibody, HT7, confirming that the pathologies comprised endogenous mouse tau without detectable human AD-tau (Supplementary Fig. 1g).

NP tau was not present when similar amounts of AD-tau were injected into the brains of younger 6-month-old APP-KI mice with minimal Aβ plaques (AD-APP-KI (6 months)) (Fig. 1d,p), suggesting that, in addition to pathological tau seeds, the formation of NP tau requires the unique Aβ plaque environment. In contrast, the NFTs that were present were likely formed through templated amplification of endogenous mouse tau independently of Aβ plaques, as has previously been demonstrated in nontransgenic mice[17]. Our experimental evidence suggesting that the NFT- and NP-like tau pathologies are distinct tau lesions is consistent with neuropathological findings from humans: whereas NFTs and NP tau are found in AD brains[19], individuals with Down syndrome (DS) only develop Aβ plaque–associated NP tau at young ages with NFTs appearing in older individuals with DS[20], and other individuals with primary age-related tauopathy (PART) only develop NFTs with few or no Aβ plaques and NP tau[21] (Supplementary Fig. 2a–c).

To further explore the relationship between Aβ plaques and NP tau pathology, we injected AD-tau into 5xFAD transgenic mice (AD-5xFAD mice), which overexpress human mutant *APP* and *PS1* genes and develop abundant AD-like Aβ plaque deposits at as early as 4 months of age[22]. Unexpectedly, unilateral injection of AD-tau (2 μg) into 8-month-old 5xFAD mice with a highly abundant Aβ plaque load (AD-5xFAD (8 months)) resulted in the development of almost exclusively $AT8^+$ NP tau at 3 m.p.i. (Fig. 1e,o,p and Supplementary Fig. 3a). Notably, $AT8^+$ NP tau was rarely observed in plaque-laden 8-month-old 5xFAD transgenic mice that were not injected or were injected with either control brain lysate or tau-immunodepleted AD-tau lysate (Supplementary Fig. 4a–d). In contrast, both NFTs and NP tau were detected at 3 m.p.i. in 5xFAD mice injected with the same dose of AD-tau at 2 months of age (AD-5xFAD (2 months)) when Aβ plaques were not yet abundant (Supplementary Fig. 3b). However, the extent of NFTs was still modest as compared to that in AD-tau-injected WT and APP-KI mice at 3 m.p.i., which had no and a relatively low burden of Aβ plaques, respectively (Fig. 1f,o and Supplementary Fig. 3b), suggesting that the induction of NP tau is positively correlated with the Aβ plaque burden and that a high plaque burden favors the induction of NP tau over NFTs (Fig. 1a–k,o–s).

NP tau aggregates faster and spreads more widely than NFT tau

To elucidate how Aβ plaques influence the induction of different types of tau pathology, we next examined the spatiotemporal spreading of NFTs and NP tau in different mouse lines from 1 to 6 m.p.i. (Fig. 2a and Supplementary Fig. 5a). Semiquantitative brain-wide mapping of tau pathologies showed that NP tau emerged as early as 1 m.p.i. in plaque-rich AD-APP-KI (15 months) and AD-5xFAD (8 months) mice and continued to increase in abundance with wider spreading throughout the hippocampus and different cortical regions from 1 to 6 m.p.i. (Fig. 2a and Supplementary Fig. 5a–e). In contrast, NFTs appeared only after 3 m.p.i. in AD-WT (15 months) and AD-APP-KI (15 months) mice, and the

distribution of NFTs was predominantly enriched in the caudal hippocampal hilus. The density of NFTs in the ipsilateral hippocampus did not increase further after 3 m.p.i. (Fig. 2a).

To confirm that the AT8$^+$ tau that was induced in our models comprised insoluble tau and that NP tau developed faster than NFT tau, sequential extraction of hippocampal tissues from AD-WT mice (with exclusively NFTs) and AD-5xFAD (8 months) mice (with exclusively NP tau) was conducted. At 1 m.p.i., sarkosyl-insoluble mouse tau was only clearly detectable in AD-5xFAD mice and not in AD-WT mice (Fig. 2b,*d*,*e*, 'P3' fraction), and this pathological tau was still significantly more abundant in AD-5xFAD mice than in AD-WT mice at 3 m.p.i. (Fig. 2c,*f*,*g*, 'P3' fraction). This likely reflects the lower abundance of NFTs in AD-WT mice than NP tau in AD-5xFAD mice at these time points. Thus, the immunohistochemical and biochemical data demonstrate more rapid induction of pathological tau in Aβ plaque–dependent NP tau than in Aβ plaque–independent NFTs.

In addition to demonstrating that the induced tau pathologies in NP tau were insoluble, we further determined that this tau was hyperphosphorylated at multiple sites relevant in AD and displayed AD-relevant misfolded conformations (Supplementary Fig. 1a,h–j). Further characterization showed that NP tau aggregates were intracellularly localized in the dystrophic axons surrounding Aβ plaques (Supplementary Fig. 6a–f), and within these axons, excitatory synaptic vesicles were particularly enriched (Supplementary Fig. 6g). Immunoelectron microscopy further confirmed the presence of abundant AD-like paired helical filaments (PHFs) in a subset of the AT8$^+$ dystrophic neurites surrounding Aβ plaques (Fig. 1n).

Mislocalized tau in periplaque dystrophic axons is critical for the facilitation of Aβ plaques on NP tau aggregation

To explore the mechanism underlying the more rapid onset and wider distribution of NP tau as compared to NFTs, we focused on the dystrophic axons surrounding Aβ plaques (Fig. 1n and Supplementary Fig. 6b). As microtubules are disrupted in such periplaque dystrophic neurites[23], it is conceivable that endogenous tau, a microtubule-binding protein, would become disengaged from microtubules and mislocalize in dystrophic axons surrounding plaques. Indeed, we detected staining for endogenous mouse tau around Aβ plaques in the brains of 8-month-old 5xFAD mice using a pan-tau antibody, K9JA, and this staining was absent in 5xFAD mice without endogenous tau expression (*Mapt*$^{-/-}$ 5xFAD mice) (Fig. 3a). This indicates that endogenous tau accumulates near plaques in the absence of exogenous pathological tau seeds. Furthermore, in 5xFAD mice without AD-tau injection, the mislocalized endogenous tau detected by K9JA was more frequently found around compact than around noncompact plaques. In AD-5xFAD mice, the induced NP tau detected by AT8 was also consistently associated more with compact plaques (Fig. 3b–e), suggesting that the soluble tau proteins mislocalized in the compact-plaque-associated dystrophic processes could be more readily recruited into NP tau aggregates once templated by misfolded tau.

To further demonstrate that the accumulated tau surrounding plaques is critical for the induction of NP tau, we generated bigenic 5xFAD mice with only one allele of the tau-encoding gene (*Mapt*$^{+/-}$ 5xFAD mice) to reduce endogenous tau levels (Fig. 3f,g), with the

expectation that there would be less tau mislocalized in the dystrophic axons surrounding Aβ plaques. Although the Aβ burden was not significantly altered by a 50% reduction of tau levels (Fig. 3h,i), AD-tau-injected *Mapt*$^{+/-}$ 5xFAD mice had less NP tau than *Mapt*$^{+/+}$ 5xFAD mice after injection with the same dose of AD-tau, as evidenced by total NP tau numbers and the amount of AT8^{+} neurites in each NP tau (Fig. 3j–l). Together, these data suggest that the threshold for seeding tau aggregation is rendered lower in dystrophic processes surrounding Aβ plaques because of increased availability of mislocalized tau.

Notably, although mislocalized tau in the periplaque dystrophic neurites appears to be 'primed' to undergo seeded aggregation, no convincing tau pathology was observed in either 5xFAD (8 months) or APP-KI (18 months) mice injected with heparin-induced tau preformed fibrils (PFFs), which are capable of inducing robust NFT-like tau inclusions in transgenic mice overexpressing mutant human tau (Supplementary Figs. 1g and 4e,f). This finding suggests that only specific conformations of tau, such as that found in pathological AD-tau, can seed mislocalized neuritic mouse tau to form NP tau aggregates.

Aβ plaque burden differentially affects the induction of NP tau and NFTs at early seeding stages

Our data are consistent with the hypothesis that the formation of NFT pathology largely depends on transport of internalized seeds to the cell soma, and the lack of NFT development in 5xFAD mice 3 months after AD-tau injection might be due to the abundance of plaque-associated dystrophic axonal terminals containing mislocalized tau that can rapidly engage with internalized AD-tau seeds, such that insufficient amounts of AD-tau seeds are available to move back into the soma and template NFT tau formation. This hypothesis is consistent with our finding that mice bearing abundant hippocampal Aβ plaques and corresponding NP tau (AD-5xFAD) invariably developed fewer NFTs in entorhinal cortex neurons that project to the hippocampus via the perforant pathway (Fig. 1l) than mice bearing fewer (AD-APP-KI) or no (AD-WT) plaques at 3 m.p.i. of AD-tau (Fig. 1p,r,s and Supplementary Fig. 1b,d,e). In addition, injection of higher amounts of AD-tau (8 μg) from two different AD brains into 5xFAD (4 months) mice resulted in the development of a larger number of NFTs than was seen in 5xFAD (4 months) mice receiving a lower dose of AD-tau (0.8 or 2 μg/mouse) (Supplementary Fig. 7). This is presumably due to AD-tau being present in excess of the amount needed for complete NP tau seeding, thereby allowing extra AD-tau to be retrogradely transported into the neuronal soma for additional NFT seeding. Thus, we believe that the relative induction of NP tau and NFTs at early seeding stages associated with Aβ plaque burden is due to the availability of internalized AD-tau seeds in dystrophic neurites and somas.

AD-tau-induced mouse NP tau in dystrophic axons triggers the formation of NFTs and NTs through secondary seeding events

Remarkably, whereas the number of NFTs plateaued in AD-WT mice at 3 m.p.i., AD-5xFAD (8 months) mice with minimal NFTs at 3 m.p.i. started to develop appreciable NFTs in the entorhinal cortex at 6 m.p.i. (Supplementary Figs. 5a,d and 8a). As injected human AD-tau is quickly degraded by 7 d post-injection *in vivo*[17], we speculate that the mouse NP tau proteins induced early in dystrophic axons are transported in retrograde to

neuronal soma, where they serve as secondary mouse tau seeds to induce formation of NFTs and NTs. To test this hypothesis, we extended the observation time in AD-5xFAD (8 months) mice to 9 m.p.i. Although only two of the six AD-5xFAD (8 months) mice survived the 9-month post-injection period, these two mice showed large numbers of NFT and NT tau pathologies that had spread throughout the brain and even to some cortical regions in which AD-WT mice showed no or rare NFTs at the same time post-injection (Supplementary Fig. 8b).

To further confirm that Aβ plaque–laden 5xFAD mice with only NP tau induction at early stages following AD-tau seeding could also develop sizable NTs and NFTs at later post-seeding stages, we repeated the time course of our AD-tau injection study in 4-month-old female 5xFAD mice that already harbored abundant Aβ plaques. Similar to older AD-5xFAD (8 months) mice, these younger mice only developed NP tau at 3 m.p.i. However, by 9 m.p.i., the abundance and intensity of NFTs and NTs detected in AD-5xFAD (4 months) mice far exceeded that observed in WT mice of a similar age injected with the same dose of AD-tau (2 μg/mouse) (Fig. 4a–d). Moreover, the NFTs that developed at 9 m.p.i. in these AD-5xFAD (4 months) mice appeared to be more misfolded and more mature than those in AD-WT (3 months) mice, as exemplified by significantly enhanced misfolded tau MC1 immunoreactivity and a higher percentage of thioflavin S–positive tau aggregates (Fig. 4b,e,f).

To directly demonstrate that NP tau could function as a secondary proteopathic seed to induce the formation of NTs and NFTs *in vivo*, WT mice were directly injected with NP tau extracted from the hippocampus of AD-5xFAD (5 months) mice at 6 m.p.i., wherein the majority of induced tau pathologies were NP tau. We observed both AD-like NTs and NFTs in multiple brain regions of all the injected WT mice at 3 m.p.i. (Fig. 4g–i). We infer that, owing to the preferential engagement of internalized AD-tau seeds with mislocalized tau accumulated in periplaque dystrophic axons, Aβ plaques initially trigger rapid NP tau formation at the expense of NFTs when AD-tau seeds are limiting. However, at later time points after AD-tau injection, NP tau can promote the formation of NFTs and NTs, likely through secondary seeding events.

To further validate our hypothesis that NP tau initiates cortical spreading of NTs and NFTs, we evaluated post-mortem human AD brain sections and focused on the visual cortex, which is one of the last brain regions to be affected in AD by tau pathology[24] and thus would be predicted to have an increased abundance of NP tau relative to NFTs. Although an almost equal abundance of NP tau and NFTs was observed in superior temporal cortex, only NP tau was observed in the visual cortex at early Braak stages of AD. At later Braak stages, NP tau and NFTs along with substantial amounts of NTs were observed in the visual cortex, although NP tau was still in greater abundance (Fig. 5). This finding was recapitulated in our AD-5xFAD (>4 months) mice, in which NP tau appeared in visual cortex as early as 3 m.p.i., followed by NFTs after 9 m.p.i. (data not shown).

The induced tau pathologies elicit effects on neural circuit activity and mouse behaviors

As NFT and NP tau pathologies are localized in distinct neuronal subcompartments, they may differentially impact neuronal function. However, these two types of tau pathology

always coexist in AD brains, such that their differential contributions to the clinical manifestations of AD were heretofore impossible to tease apart. Thus, using our new model systems, we sought to elucidate the functional consequences of these distinct tau pathologies by performing a series of behavioral tests on four cohorts of mice: AD-5xFAD (5 months) mice at 1 and 3 m.p.i. (exclusively NP tau), AD-WT (5 months) mice at 3 m.p.i. (exclusively NFTs), AD-5xFAD (2 months) mice at 3 m.p.i. (with both NP tau and NFTs) and noninjected age-matched littermates of the corresponding genotype used as controls. Mice harboring NFTs, NP tau or both pathologies all showed normal exploratory activities in the open field test (Fig. 6a,b and Supplementary Fig. 9a). Interestingly, mice with NFTs (both AD-WT (5 months) and AD-5xFAD (2 months)), but not mice with NP tau (AD-5xFAD (5 months)), spent less time in the open areas of the elevated zero maze (Fig. 6a,c and Supplementary Fig. 9b), and AD-WT (5 months) mice also displayed increased freezing behavior even before the stimulation in the contextual fear conditioning test (Fig. 6e), suggesting that NFTs impair resident ventral hippocampal neurons, leading to elevated levels of anxiety-related behaviors; this is consistent with the reported role of ventral hippocampus in emotional processing[25]. On the other hand, all AD-tau-injected mice performed as well as control mice in the spontaneous alternation Y-maze test (Fig. 6a,d and Supplementary Fig. 9c) and showed levels of freezing equivalent to those of control mice in the contextual fear conditioning test at 1 d post-stimulation (Fig. 6e), suggesting that these mice have largely normal short-term and long-term memory acquisition. However, mice with NP tau (AD-5xFAD (5 months) mice at both 1 and 3 m.p.i.) displayed a considerable reduction in freezing levels from 1 to 14 d after stimulation in the fear conditioning test, indicating that mice with exclusively NP tau pathology have impaired remote memory retention (Fig. 6e and Supplementary Fig. 9d). Given the wider distribution of NP tau, we speculate that this NP tau–associated behavior deficiency might be a global outcome in contrast to the local circuitry impairment associated with NFTs. Although the AD-5xFAD (2 months) mice had both NFTs and NP tau, they did not show deficits in contextual fear conditioning like the AD-WT (5 months) or AD-5xFAD (5 months) mice (Supplementary Fig. 9d), possibly owing to lower amounts of each type of tau pathology (Fig. 1o,p).

Finally, we examined the functional consequences of NFTs and NP tau on neural circuit activity within the perforant pathway by performing voltage-sensitive dye recording on hippocampal slices taken from WT (5 months) and 5xFAD (5 months) mice with or without AD-tau injection at 3 m.p.i. AD-WT mice showed increased neuronal activity in the hippocampus as compared to control WT mice in response to stimulation of the perforant pathway, whereas AD-5xFAD mice did not show this change (Fig. 6f–h), indicating that NFTs alone cause impairment in neuronal circuit activity. However, it is difficult to tease apart the contribution of NP tau pathology owing to the presence of confounding Aβ plaques and the wider spatial distribution of NP tau. Overall, the combined histological and functional data indicate distinct manifestations of tau pathology during the progression of AD: NP tau initiates and promotes the spreading of distinct types of tau pathology to different brain regions, whereas NFTs largely impair the neurons harboring them, leading to dysfunction of the associated neural circuitry and behavioral deficiency.

DISCUSSION

By injecting human AD-tau into the brains of plaque-bearing transgenic mice, we have generated the most pathologically relevant AD mouse model to date, which harbors Aβ plaques and all three types of tau pathology (NP tau, NFTs and NTs) found in AD brains. We also provide, to our knowledge, the first experimental evidence that Aβ plaques create an environment that allows for rapid seeded induction of tau pathology from endogenous mouse tau. Although the original amyloid cascade hypothesis specified a link between Aβ and the formation of NFTs[1], it is possible that this linkage is not entirely direct and that plaque-associated cells (i.e., microglia) or molecules[23,26,27] may also be involved. Moreover, injections of Aβ do not directly induce a convincing tau pathology[28–32]. A recent study proposes that Aβ enhances tau pathogenesis through increasing the formation of certain tau species capable of seeding new aggregates[16], but the identity of such tau species and the underlying mechanism are still poorly understood. Our model suggests a multistep mechanism of Aβ plaque–mediated tau pathogenesis (Supplementary Fig. 10): in early disease stages, Aβ plaques cause an accumulation of endogenous tau within dystrophic axons surrounding the plaques to create a unique environment that facilitates the rapid recruitment of tau into fibrils as NP tau by small amounts of proteopathic tau seeds. Thereafter, the aggregated tau in NP tau becomes an enriched source of secondary tau seeds, which may be translocated via axons to neuronal somas and dendrites where endogenous soluble tau is recruited to form NFTs and NTs at later disease stages. In addition, Aβ plaques may enhance and sustain tau pathologies through additional mechanisms, such as impairment of intracellular protein degradation[33].

Notably, our study suggests that Aβ plaques are necessary but not sufficient to initiate the cascade of pathological tau transmission, as misfolded tau seeds with the correct conformations are also required to trigger this process. Moreover, our findings support a mechanism whereby Aβ plaques unleash the spread of NFTs from the medial temporal lobe more widely into neocortical areas during the progression of AD, as evidenced by both post-mortem neuropathological data[4] and recent positron emission tomography (PET) imaging studies[5–9]. In human brains, age-related NFTs that develop in the medial temporal lobe independently of Aβ plaques likely provide the initial source of pathological tau seeds. We infer that these proteopathic tau seeds are either locally released or intracellularly transported from the NFT-bearing neuronal perikarya in the medial temporal lobe to areas harboring senile plaques where dystrophic neurites around Aβ plaques allow for the rapid formation of NP tau at early stages of AD. The NP tau could then possibly trigger the formation of NFTs in connected but distantly localized neuronal somas at later stages. Through such iterative cycles of pathological tau amplification, NP tau and NFTs then appear to spread from the initial regions (i.e., medial temporal lobe) to other connected regions and ultimately throughout the cortex, accompanied by substantial cognitive dysfunction in individuals with AD.

The new mouse models of AD with both Aβ plaques and tau pathologies described here will enable further interrogation of the enigmatic link between Aβ plaques and tau pathology in AD progression. Furthermore, these mice will be extremely useful in testing therapies that

target one or both pathologies to determine whether combination therapy will be required or if monotherapy targeting one or the other will eliminate both pathologies.

ONLINE METHODS

Mice

$APP^{NL-F/NL-F}$ KI mice on the C57BL/6 background were obtained from T. Saido; the mice used in the experiments were the third generation of the mice originally obtained from T. Saido's group (RIKEN Brain Science Institute, Japan). 5xFAD transgenic mice (Tg6799 line) were bred with B6/SJL F_1 mice, and both 5xFAD and tau-knockout mice were purchased from Jackson Lab. $Mapt^{+/-}$ and $Mapt^{-/-}$ 5xFAD mice were generated by crossbreeding 5xFAD transgenic mice with tau knockouts, and the F_1 mice were used in the study. Genotyping was performed according to the vendor's instructions. The primers used for PCR genotyping were as follows: for 5xFAD mice: PS1_F 5′-AATAGAGAACGGCAGGA GCA-3′, PS1_R, 5′-GCCATGAGGGCACTAATCAT-3′; Internal ctrl-1_F 5′-CTAGGCCACAGAATTGAAAGATCT-3′, Internal ctrl-1_R 5′-GTAGGT GGAAATTCTAGCATCATCC-3′; APP_F 5′-AGGACTGACCACTCGACCAG-3′, APP_R 5′-CGGGGGTCTAGTTCTGCAT-3′; Internal ctrl-2_F 5′-CAAAT GTTGCTTGTCTGGTG-3′, Internal ctrl-2_R 5′-GTCAGTCGAGTGCAC AGTTT-3′; for $APP^{NL-F/NL-F}$ KI mice: APP-KI_E16WT_F 5′-ATCTCGGAAGT GAAGATG-3′, APP-KI_E16WT_R 5′-TGTAGATGAGAACTTAAC-3′; APP-KI_E16MT_F 5′-ATCTCGGAAGTGAATCTA-3′, APP-KI_LoxP_R 5′-C GTATAATGTATGCTATACGAAG-3′; for tau knockouts: Tau-KO E1_F 5′-GC CAGAGGCCACTTGTGTAG-3′, WT_F 5′-AATGGAAGACCATGCTGGAG-3′; Shared Tau-KO and WT_R 5′-ATTCAACCCCCTCGAATTTT-3′.

Aged nontransgenic C57BL/6 mice were either purchased from Charles River or obtained from a breeding colony maintained in our center. Both male and female mice were used in these studies. All animals were allocated randomly for histological experiments, but groups were counterbalanced for animal sex and group average body weight. All animal protocols were approved by the University of Pennsylvania's Institutional Animal Care and Use Committee (IACUC).

Purification of tau paired helical filaments from Alzheimer's disease brains

Two sporadic AD brains, one Down syndrome–derived AD brain with abundant tau pathology and two age-matched control brains with histological confirmation were used in this study (Supplementary Table 1). AD-tau isolation was conducted as described[17]. The brain extracts from the two age-matched normal controls were generated using the same protocol. The total protein concentrations of the final supernatant fractions were analyzed using a BCA assay (Fisher); tau, Aβ40, Aβ42 and α-synuclein (α-syn) concentrations were estimated by sandwich ELISA for each protein or peptide. The concentration of purified tau from AD brains in each preparation was 1.5–2.3 mg/ml with a purity of 15–27.7%, accompanied by Aβ42 levels of 0.07–0.47 μg/ml. Aβ40 levels ranged from undetectable to 0.07 μg/ml, and α-syn levels were 0.92–4.95 μg/ml. The concentration of tau from control normal brains in each preparation was 2–5 ng/ml with a purity of 0.016–0.049%,

accompanied by Aβ42 ranging from undetectable to 0.01 μg/ml, Aβ40 at levels of 0.002–0.004 μg/ml and α-syn at levels of 5.8–7.6 μg/ml.

Recombinant human tau purification and *in vitro* fibrillization

The recombinant human full-length tau isoform T40 used in these studies was expressed in BL21 (DE3) RIL cells and was purified by cationic exchange using fast protein liquid chromatography (FPLC) as previously described[35]. Tau PFFs were made as previously described[36].

Sandwich ELISA

The concentrations of tau, α-syn, Aβ40 and Aβ42 in AD-tau preparations were measured using sandwich ELISAs as previously described[37,38].

Stereotaxic surgery

Mice were deeply anesthetized with ketamine–xylazine–acepromazine, immobilized in a stereotaxic frame (David Kopf Instruments) and aseptically inoculated with human brain extracts or synthetic tau PFFs in the dorsal hippocampus and overlying cortex of one hemisphere (bregma: −2.5 mm; lateral: +2 mm; depth: −2.4 mm and −1.4 mm from the skull) using a Hamilton syringe as described. Each of the two injection sites received 2.5 μl of inoculum, with AD-tau prepared at 0.4 μg tau/μl (1 μg tau/site), or the synthetic tau PFFs prepared at 1.8 μg tau/μl (4.5 μg tau/site), and materials were injected into the hippocampus first (−2.4 mm from the skull) before the needle was pulled vertically upwards to the cortical injection site (−1.4 mm from the skull). The body temperature of the mice was maintained at 37 °C with a heating pad during and after surgery until mice were awake for 2 h. To examine the spreading pattern of pathologies *in vivo*, all the mice were unilaterally injected in the right hemisphere, with a total amount of 2 μg AD-tau. For biochemical extraction and behavior tests, all the mice were bilaterally injected in both hemispheres, with a total amount of 4 μg AD-tau. For the *in vivo* seeding experiment, hippocampi in WT mice were bilaterally injected with control lysate or 0.4 μg NP-tau per side. The amounts of total protein in control lysate and NP-tau lysate were similar.

Generation of mouse-tau-specific polyclonal antibody

Mouse-tau-selective polyclonal antibody R2295 was generated by immunizing rabbits with recombinant mouse 4R2N full-length tau (Covance Research Products, Inc., Denver, CO). To remove antibodies against human tau, the antiserum was first applied to an N-hydroxysuccinimide (NHS)-activated agarose column (Pierce) coupled to recombinant full-length human tau. This process was performed twice, and the flow-through from the second pass was affinity purified using an NHS-activated agarose column coupled to recombinant full-length mouse tau. The eluates from the mouse-tau-coupled column were verified to be specific to mouse tau by western blotting of recombinant tau and immunostaining of cells expressing mouse or human tau. As the major difference in amino acid sequence between human and mouse tau is located at the N terminus, the epitopes of the mouse-tau-specific antibodies are likely located at the N terminus.

Immunohistochemistry and immunofluorescence

Mice were killed and processed as previously described[36]. The immunostainings were performed on 6-μm paraffin-embedded mouse brain sections. The quantifications of the percentage of area occupied by different immunoreactive tau pathologies were performed with HALO software (Indica Labs). $AT8^+$ NP tau and NFTs were quantified through blinded manual counting from eight coronal sections (bregma 0.98 mm, −0.22 mm, −1.22 mm, −2.18 mm, −2.92 mm, −3.52 mm, −4.48 and −5.52 mm) for each mouse; tau pathology was determined on the basis of morphology. We defined each $AT8^+$, $AT180^+$, or $MC1^+$ area surrounding a single nucleus as an NFT and each cluster of granule that was $AT8^+$, $AT180^+$, or $MC1^+$ without a single central nucleus as an NP.

Gallyas silver staining

After sections were deparaffinized and hydrated, they were put in 5% periodic acid for 5 min and then washed twice in distilled water (dH_2O) for 5 min each time. The sections were incubated with silver iodide solution (12 g sodium hydroxide, 30 g potassium iodide and 10.5 ml 1% silver nitrate, with dH_2O added to 300 ml) for 1 min and placed in 0.5% acetic acid for 5 min twice. After rinsing in dH_2O, the sections were developed in developer solution mixed with solutions A, B and C. Solution A contained 50 g anhydrous sodium carbonate in 1,000 ml dH_2O, solution B contained 1.9 g ammonium nitrate, 2 g nitrate and 10 g tungstosilicic acid in 1,000 ml dH_2O and solution C contained 1.9 g ammonium nitrate, 2 g silver nitrate, 10 g tungstosilicic acid and 7.6 ml 37% formaldehyde in 1,000 ml dH_2O. The reaction was stopped in 0.5% acetic acid for 5 min.

Immunoelectron microscopy

Brain tissues were first fixed in periodate–lysine–paraformaldehyde (PLP) buffer (2% paraformaldehyde + 0.075 M lysine + 0.01 M sodium *m*-periodate in 0.037 M $NaPO_4$ buffer, pH 7.0) for 4 h and then washed with 50 μM NH_4Cl in PBS and stored in 5% sucrose in PBS + 0.05% thimerosal. The tissues were then sectioned by vibratome at a thickness of 50–60 μm, permeabilized for 30 min in 50% ethanol and blocked for 30 min in PBS + 2% fish gelatin + 0.0005% saponin + 0.05% thimerosal (PBS–FG–sap). Sections were incubated with monoclonal antibody AT8 (at a dilution of 1:1,000 or 1:4,000) for 3 d and then overnight with biotinylated horse anti–mouse IgG, followed by overnight incubation in ABC Elite avidin–HRP conjugate (Vector Laboratories, Burlingame, CA). All incubations were conducted in PBS–FG–sap at room temperature, and HRP was detected with 10 mg/ml 3,3′-diaminobenzidine (DAB) in 0.1 M Tris, pH 7.4, and 10 mM imidazole after incubation for 15 min at room temperature. The stained tissues were post-fixed for 90 min in 1% OsO_4 + 1.5% potassium ferrocyanide in 0.05 M cacodylate buffer, pH 7.4, and then dehydrated in ethanol and embedded in EMbed 812 (Electron Microscopy Sciences, Hatfield, PA). Selected 2-μm semithin sections were re-embedded and cut for electron microscopy. Sections were stained with 1% uranyl acetate in 50% ethanol and Reynolds lead citrate or with lead citrate only.

Biochemical sequential extraction from mouse brains

Mouse brains were removed from AD-WT or 5xFAD mice at the designated time points. Different regions, including hippocampus and cortex, were dissected separately and first snap frozen in dry ice and then stored at −80 °C before extraction. For detecting the pathological insoluble tau induced in mice, sequential extractions were performed as follows: hippocampal tissue from each mouse was individually homogenized in 9 volumes per gram tissue with cold high-salt RAB buffer (0.75 M NaCl, 100 mM Tris, 1 mM EGTA, 0.5 mM $MgSO_4$, 0.02 M NaF, 2 mM DTT, containing protease inhibitor cocktail, phosphatase inhibitor and phenylmethyl-sulfonyl fluoride (PMSF), pH 7.4), sonicated and designated as homogenate. The homogenates were centrifuged at 100,000*g* for 30 min at 4 °C. The supernatants were saved as the 'high-salt supernatant' fraction (S1), whereas pellets were resonicated in high-salt RAB buffer containing 1% Triton X-100, protease inhibitor cocktail, phosphatase inhibitor and PMSF, and centrifuged again at 100,000*g* for 30 min at 4 °C. The resulting supernatants were saved as the 'Triton-soluble' fraction (S2), and the pellets were resonicated in PHF buffer (10 mM Tris, 0.8 M NaCl, 1 mM EDTA, 2 mM DTT, 10% sucrose, containing 1% sarkosyl, protease inhibitor cocktail, phosphatase inhibitor and PMSF, pH 7.4) and rotated at room temperature for 1 h before being centrifuged again at 100,000*g* for 30 min at 4 °C. The resulting supernatants were saved as the 'sarkosyl-soluble' fraction (S3), and the pellets were washed once with PBS and then resuspended in PBS at one-tenth of the initial volume and sonicated to clear the solution; supernatants were saved as the 'sarkosyl-insoluble' fraction (P3).

To extract NP-tau from 5xFAD mice for further *in vivo* seeding experiments, hippocampi were dissected from AD-5xFAD (5 months) mice at 6 m.p.i. The tissues were homogenized with 9 volumes of PBS with 0.1% sarkosyl, the homogenates were centrifuged at 10,000*g* for 10 min, the low-spin pellets were discarded and the supernatants were further centrifuged at 100,000*g* for 45 min. The higher-spin pellets were then washed twice with PBS and finally resuspended in a small volume of PBS for injection. The yield of final insoluble NP tau was less than 60 ng/μl. All the PBS used in our experiments was Ca^{2+} and Mg^{2+} free.

Western blotting and dot blotting

For western blotting, homogenates (~50–60 μg protein) from each experimental group and an equal proportion of corresponding Ho, S1, S2 and S3, as well as 20-fold enrichment of P3 relative to Ho, were loaded on SDS–PAGE gels and transferred to 0.22-μm nitrocellulose membranes. For dot blotting, an equal amount of P3 roughly estimated from the western blots were loaded onto 0.22-μm nitrocellulose membranes through Bio-Dot Microfiltration Apparatus (Bio-Rad) and washed twice with TBS buffer. The nitrocellulose membranes were then blocked in Odyssey blocking buffer (Li-Cor Biosciences) or 5% milk diluted in TBS before being immunoblotted with specific primary antibodies (Supplementary Table 2). The blots were further incubated with IRDye-labeled secondary antibodies and scanned using ODY-2816 Imager. The optical densities were measured with Image Studio software (Li-Cor Biosciences). The full-length gels for the cropped blots shown in the main figures are presented in Supplementary Figure 11.

Immunodepletion of Tau from AD-tau preparations

Anti-tau antibodies R2295, Tau5 and K9JA were covalently conjugated to Dynabeads M-280 Tosylactivated (Fisher Scientific) per the manufacturer's instructions and then mixed for use. Immunodepletion of tau was performed by incubating 200 μl of diluted AD-tau preparations containing 15 μg tau with anti-tau antibody–bead complexes containing 60 μg total antibodies overnight at 4 °C with rotation. The unbound fraction in each immunodepletion round was separated from the antibody–bead complex using a magnet and was incubated again with the same amount of anti-tau antibody six times in total. Mock immunodepletion was performed using a control mouse IgG1 antibody that did not recognize tau. The AD lysates immunodepleted with anti-tau antibodies contained 0.61 ng/μl tau, whereas the mock immunodepletion AD lysate contained 24 ng/μl tau. 7.5 μl final lysates immunodepleted with or without anti-tau antibodies was unilaterally injected into the hippocampus of each 5xFAD (11 months) mouse.

Histology

In mouse brain sections, semiquantitative analyses of NP tau were performed as previously described[36], whereby the extent of $AT8^+$ NP tau induced at 1, 3 and 6 m.p.i. was graded as 0–3 (0, no pathology; 3, high pathology) at eight coronal sections (bregma 0.98 mm, −0.22 mm, −1.22 mm, −2.18 mm, −2.92 mm, −3.52 mm, −4.48 and −5.52 mm) for each mouse. Averaged scores from the three mice at each time point (except $n = 2$ for AD-WT at 1 m.p.i.) were imported into a customized software to create heat maps representing the amount and distributions of NP tau. AD-like NFTs, indicated by blue dots, were manually added onto the heat maps based on the amount and distribution of $AT8^+$ AD-like NFT staining. The axonal $AT8^+$ NTs immunostained in corpus callosum and fimbria regions are presented as purple lines.

In human brain tissues, semiquantitative analyses of tau pathologies in the form of NFTs and NP tau were estimated by PHF-1 immunohistochemistry, and the amount of Aβ senile plaques was determined semiquantitatively by NAB228 immunohistochemistry. The pathologies were graded as 0–3 (0, no pathology; 3, high pathology) by two blinded individuals; results were similar. The cases examined from individuals with AD, DS or PART are listed in Supplementary Table 2.

Behavior tests

To evaluate the effects of two types of tau pathology at the behavior level, 5xFAD mice (5 months or 2 months) and nontransgenic WT littermates (5 months) with or without AD-tau injection at 3 m.p.i. were sequentially tested in the open field test, elevated zero maze, Y-maze and contextual fear conditioning. All the tests were conducted from 7:30–11:00 a.m. in the lights-on cycle by experimenters blinded to group designation. Mice were habituated to the procedure room 30 min before each test. The 5xFAD (5 months) mice used in the test at 3 m.p.i. were all female and were all male in the test at 1 m.p.i. 5xFAD (2 months) mice and the nontransgenic WT littermates were of mixed sex with roughly similar ratios in both the control and AD-tau-injected groups.

Open field—To assess general activity, locomotion and anxiety-related behavior, mice were tested in an open field arena (36 × 36 cm) (San Diego Instruments Photobeam Activity System) with clear Plexiglas walls and a white floor that was evenly illuminated. Mice were individually placed in the center and allowed to freely explore for 10 min. The total number of center, peripheral and vertical beam breaks was automatically recorded by tracking software as a direct measure of locomotion and activity.

Elevated zero maze—A 5.5-cm-wide circular track with an external diameter of 45 cm that was raised 40 cm above the floor (San Diego Instruments) was used. The track had two open and two walled segments of equal dimensions. Mice were gently placed in the center of a closed segment to begin a 5-min trial and were recorded by video. The time in open areas was defined as time when mice put both of their hind limbs in the open areas and was estimated by a person blinded to mouse groups with a timer. Mice that jumped off the platform twice continuously were excluded from the analysis.

Y-maze—To measure short-term working memory, mice were tested for spontaneous alternation behavior (SAB) in a Y-shaped maze (San Diego Instruments) using a standard protocol[39]. SAB during an 8-min test period was calculated as the proportion of alternations (an arm choice differing from the previous two choices to the total number of alternation opportunities (total arm entries, 2)). Mice that jumped off the platform twice continuously were excluded from the analysis.

Contextual fear conditioning—Contextual conditioning is a hippocampus-dependent form of learning in which a unique environment is associated with an aversive stimulus (foot shock). Mice were handled for 1–2 min per day for 3 d before training. For training, mice were individually placed in a conditioning chamber (Med Associate) within a sound-attenuating cabinet, and a 2-s foot shock was delivered at 148–150 s of a 180-s training phase. For the relatively younger cohorts of AD-5xFAD (2 months) mice at 3 m.p.i. and AD-5xFAD (5 months) mice at 1 m.p.i., the stimulation strength was 1.25 mA, and for the older cohorts of AD-WT (5 months) mice at 3 m.p.i. and AD-5xFAD (5 months) mice at 3 m.p.i. the stimulation strength was 1.75 mA. To assess learning, at 1 d and again at 14 d after training, mice were returned to the same conditioning chamber for a 5-min exposure without any stimulation. Time spent freezing (motionless except for respiratory movements) in the chamber was automatically assessed by the camera and Freezscan software (Clever Systems).

Recording of hippocampal circuit activity

To evaluate the effects of AD-like NFT and NP tau pathologies on neural circuit activity, changes in regional membrane potential were measured using voltage-sensitive dye imaging in hippocampal brain slices prepared from all groups of the mice subjected to behavioral tests. An extracellular stimulation was administered to the perforant pathway, and signals generated in response to this stimulus were recorded in various components of the hippocampal slice, including the dentate gyrus, hilus and area CA3. The experiments were done and analyzed by two researchers blinded to the identities of the groups.

Brain slice preparation—Brains were removed and blocked in ice-cold artificial cerebrospinal fluid (ACSF) (in mM: 130 sucrose, 3 KCl, 1.25 $NaHPO_4$, 1 $MgCl_2$, 2 $CaCl_2$, 26 $NaHCO_3$ and 10 dextrose), in which NaCl was replaced with an equal osmolar concentration of sucrose. Hippocampal slices (350 μm) were cut at 12° off horizontal with a vibrating tissue slicer (VT1200S, Leica, Deerfield, IL). Vibratome cuts at this angle provide three to four optimal slices with well-preserved hippocampal–entorhinal cortical connections per mouse. A cut was made between the CA1 and CA3 subfields to eliminate the possibility of recording reverberations from CA3 and disynaptic activation via the perforant path projection to CA3. Slices were allowed to recover in a static interface chamber at 34 °C for 30 min and then stored at room temperature for up to 6 h.

Voltage-sensitive dye imaging—Voltage-sensitive dye fluorescence signals were captured with a high-speed 80 × 80 pixel charge-coupled device (CCD) camera (NeuroCCD-SM, Redshirt Imaging) at a 1,000-Hz frame rate. We used a collimated light-emitting diode emitting with peak intensity at 505 nm (LEDC9, ThorLabs) to excite the voltage-sensitive dye (di-3-ANEPPDHQ). Voltage-sensitive dye imaging was achieved through collecting emitted fluorescence by using a Chroma U-N41002 (Chroma Technology) filter cube, comprising an excitation filter (535 nm/50 nm), an emission filter (610 nm/70 nm) and a dichroic mirror (565 nm-LP). All filter widths are given as the full width at half maximum. For stimulation of the granule cell layer, a bipolar tungsten stimulating electrode was placed adjacent to the hippocampal fissure between the suprapyramidal blade and apex of the granule cell layer to activate the perforant pathway. Electrical stimulation and onset of imaging trials were controlled by an electrical trigger with a delay of 200 ms before stimulus onset to obtain a baseline for imaging analysis. Repeated measurements of 12 trials were taken, and trials were averaged to increase the signal-to-noise ratio.

Data analysis—All analysis was performed in IGOR (WaveMetrics, Lake Oswego, OR) on averages of 12 trials. A reference frame was calculated as the average of 40 frames (0.4-ms integration time) preceding the stimulation. The data were displayed as the change in fluorescence divided by the resting fluorescence (ΔF/F). This minimizes variations in the signal attributable to differences in dye concentration and illumination intensity. To compensate for photobleaching, fitted double exponentials were subtracted from normalized ΔF/F. A depolarization of membrane potential produces a reduction in ΔF/F, or a downward deflection. To be consistent with electrophysiological conventions, ΔF/F signals were inverted so that depolarizations were displayed as positive signals (warmer colors) and hyperpolarizations were represented as negative signals (colder colors). Local voltage-sensitive dye signals were quantified from regions of interest in stratum dentate gyrus, hilus and CA3.

Statistics

A two-tailed *t*-test was performed when two groups were compared and one-way ANOVA or two-way ANOVA with repeated measures was performed when multiple groups were compared, according to different conditions. Statistical analyses were mostly performed with Prism software (GraphPad Software, Inc.). Differences were considered significant at $*P \leq 0.05$, $**P \leq 0.01$ and $***P \leq 0.001$. Sample size was determined on the basis of previous

experience. Detailed statistical information for all the data presented in this study is listed in Supplementary Table 3.

Life Sciences Reporting Summary

Further information on experimental design and reagents is available in the **Life Sciences Reporting Summary**.

Data availability

The data that support the findings of this study are available from the corresponding author upon reasonable request. Uncropped immunoblot images are available in Supplementary Figure 11.

Supplementary Material

Refer to Web version on PubMed Central for supplementary material.

Acknowledgments

We thank S. Kim, B. Zoll, H. Brown, F. Bassil, J. Robinson, T. Schuck and M. Byrne for technical assistance. We thank W. O'Brien and the Penn Neurobehavioral Testing Core for help with behavior tests, S. Xie for help with statistical analyses and E. Lee for helpful comments. We thank N. Kanaan (Michigan State University) for providing TOC1 antibody, which was generated and initially provided by L. Binder (deceased), P. Davies (Hofstra Northwell School of Medicine) for contributing PHF1, MC1 and TG3 antibodies, and M. Goedert (University of Cambridge) for contributing pS422 antibody. T. Saido (RIKEN Brain Science Institute) is thanked for providing APP-KI mice. This work was funded by National Institute on Aging (NIA) AG10124 (J.Q.T.), AG17586 (V.M.-Y.L.), AG017628 (T.A.), CurePSP (J.Q.T.) and the Woods Foundation (V.M.-Y.L.).

References

1. Hardy JA, Higgins GA. Alzheimer's disease: the amyloid cascade hypothesis. Science. 1992; 256:184–185. [PubMed: 1566067]
2. Gómez-Isla T, et al. Neuronal loss correlates with but exceeds neurofibrillary tangles in Alzheimer's disease. Ann Neurol. 1997; 41:17–24. [PubMed: 9005861]
3. Bennett DA, Schneider JA, Wilson RS, Bienias JL, Arnold SE. Neurofibrillary tangles mediate the association of amyloid load with clinical Alzheimer disease and level of cognitive function. Arch Neurol. 2004; 61:378–384. [PubMed: 15023815]
4. Braak H, Thal DR, Ghebremedhin E, Del Tredici K. Stages of the pathologic process in Alzheimer disease: age categories from 1 to 100 years. J Neuropathol Exp Neurol. 2011; 70:960–969. [PubMed: 22002422]
5. Schöll M, et al. PET imaging of tau deposition in the aging human brain. Neuron. 2016; 89:971–982. [PubMed: 26938442]
6. Schwarz AJ, et al. Regional profiles of the candidate tau PET ligand 18F-AV-1451 recapitulate key features of Braak histopathological stages. Brain. 2016; 139:1539–1550. [PubMed: 26936940]
7. Sepulcre J, et al. In vivo tau, amyloid, and gray matter profiles in the aging brain. J Neurosci. 2016; 36:7364–7374. [PubMed: 27413148]
8. Brier MR, et al. Tau and Aβ imaging, CSF measures, and cognition in Alzheimer's disease. Sci Transl Med. 2016; 8:338ra66.
9. Wang L, et al. Evaluation of tau imaging in staging Alzheimer disease and revealing interactions between β-amyloid and tauopathy. JAMA Neurol. 2016; 73:1070–1077. [PubMed: 27454922]
10. Götz J, Chen F, van Dorpe J, Nitsch RM. Formation of neurofibrillary tangles in P301L tau transgenic mice induced by Aβ42 fibrils. Science. 2001; 293:1491–1495. [PubMed: 11520988]

11. Lewis J, et al. Enhanced neurofibrillary degeneration in transgenic mice expressing mutant tau and APP. Science. 2001; 293:1487–1491. [PubMed: 11520987]
12. Bolmont T, et al. Induction of tau pathology by intracerebral infusion of amyloid-β-containing brain extract and by amyloid-β deposition in APP × Tau transgenic mice. Am J Pathol. 2007; 171:2012–2020. [PubMed: 18055549]
13. Clavaguera F, et al. Transmission and spreading of tauopathy in transgenic mouse brain. Nat Cell Biol. 2009; 11:909–913. [PubMed: 19503072]
14. Hurtado DE, et al. Aβ accelerates the spatiotemporal progression of tau pathology and augments tau amyloidosis in an Alzheimer mouse model. Am J Pathol. 2010; 177:1977–1988. [PubMed: 20802182]
15. Pooler AM, et al. Amyloid accelerates tau propagation and toxicity in a model of early Alzheimer's disease. Acta Neuropathol Commun. 2015; 3:14. [PubMed: 25853174]
16. Bennett RE, et al. Enhanced tau aggregation in the presence of amyloid β. Am J Pathol. 2017; 187:1601–1612. [PubMed: 28500862]
17. Guo JL, et al. Unique pathological tau conformers from Alzheimer's brains transmit tau pathology in nontransgenic mice. J Exp Med. 2016; 213:2635–2654. [PubMed: 27810929]
18. Saito T, et al. Single *App* knock-in mouse models of Alzheimer's disease. Nat Neurosci. 2014; 17:661–663. [PubMed: 24728269]
19. Nelson PT, Braak H, Markesbery WR. Neuropathology and cognitive impairment in Alzheimer disease: a complex but coherent relationship. J Neuropathol Exp Neurol. 2009; 68:1–14. [PubMed: 19104448]
20. Mann DM, Esiri MM. The pattern of acquisition of plaques and tangles in the brains of patients under 50 years of age with Down's syndrome. J Neurol Sci. 1989; 89:169–179. [PubMed: 2522541]
21. Crary JF, et al. Primary age-related tauopathy (PART): a common pathology associated with human aging. Acta Neuropathol. 2014; 128:755–766. [PubMed: 25348064]
22. Oakley H, et al. Intraneuronal β-amyloid aggregates, neurodegeneration, and neuron loss in transgenic mice with five familial Alzheimer's disease mutations: potential factors in amyloid plaque formation. J Neurosci. 2006; 26:10129–10140. [PubMed: 17021169]
23. Sadleir KR, et al. Presynaptic dystrophic neurites surrounding amyloid plaques are sites of microtubule disruption, BACE1 elevation, and increased Aβ generation in Alzheimer's disease. Acta Neuropathol. 2016; 132:235–256. [PubMed: 26993139]
24. Montine TJ, et al. National Institute on Aging–Alzheimer's Association guidelines for the neuropathologic assessment of Alzheimer's disease: a practical approach. Acta Neuropathol. 2012; 123:1–11. [PubMed: 22101365]
25. Bannerman DM, et al. Regional dissociations within the hippocampus—memory and anxiety. Neurosci Biobehav Rev. 2004; 28:273–283. [PubMed: 15225971]
26. Wang Y, et al. TREM2-mediated early microglial response limits diffusion and toxicity of amyloid plaques. J Exp Med. 2016; 213:667–675. [PubMed: 27091843]
27. Yuan P, et al. TREM2 haplodeficiency in mice and humans impairs the microglia barrier function leading to decreased amyloid compaction and severe axonal dystrophy. Neuron. 2016; 90:724–739. [PubMed: 27196974]
28. Meyer-Luehmann M, et al. Extracellular amyloid formation and associated pathology in neural grafts. Nat Neurosci. 2003; 6:370–377. [PubMed: 12598899]
29. Meyer-Luehmann M, et al. Exogenous induction of cerebral β-amyloidogenesis is governed by agent and host. Science. 2006; 313:1781–1784. [PubMed: 16990547]
30. Eisele YS, et al. Peripherally applied Aβ-containing inoculates induce cerebral β-amyloidosis. Science. 2010; 330:980–982. [PubMed: 20966215]
31. Langer F, et al. Soluble Aβ seeds are potent inducers of cerebral β-amyloid deposition. J Neurosci. 2011; 31:14488–14495. [PubMed: 21994365]
32. Rosen RF, et al. Exogenous seeding of cerebral β-amyloid deposition in βAPP-transgenic rats. J Neurochem. 2012; 120:660–666. [PubMed: 22017494]

33. Almeida CG, Takahashi RH, Gouras GK. β-amyloid accumulation impairs multivesicular body sorting by inhibiting the ubiquitin–proteasome system. J Neurosci. 2006; 26:4277–4288. [PubMed: 16624948]

34. Montine TJ, et al. Multisite assessment of NIA-AA guidelines for the neuropathologic evaluation of Alzheimer's disease. Alzheimers Dement. 2016; 12:164–169. [PubMed: 26327235]

35. Li W, Lee VM. Characterization of two VQIXXK motifs for tau fibrillization *in vitro*. Biochemistry. 2006; 45:15692–15701. [PubMed: 17176091]

36. Iba M, et al. Synthetic tau fibrils mediate transmission of neurofibrillary tangles in a transgenic mouse model of Alzheimer's-like tauopathy. J Neurosci. 2013; 33:1024–1037. [PubMed: 23325240]

37. Guo JL, Lee VM. Seeding of normal tau by pathological tau conformers drives pathogenesis of Alzheimer-like tangles. J Biol Chem. 2011; 286:15317–15331. [PubMed: 21372138]

38. Lee EB, Skovronsky DM, Abtahian F, Doms RW, Lee VM. Secretion and intracellular generation of truncated Aβ in β-site amyloid-β precursor protein–cleaving enzyme expressing human neurons. J Biol Chem. 2003; 278:4458–4466. [PubMed: 12480937]

39. King DL, Arendash GW. Behavioral characterization of the Tg2576 transgenic model of Alzheimer's disease through 19 months. Physiol Behav. 2002; 75:627–642. [PubMed: 12020728]

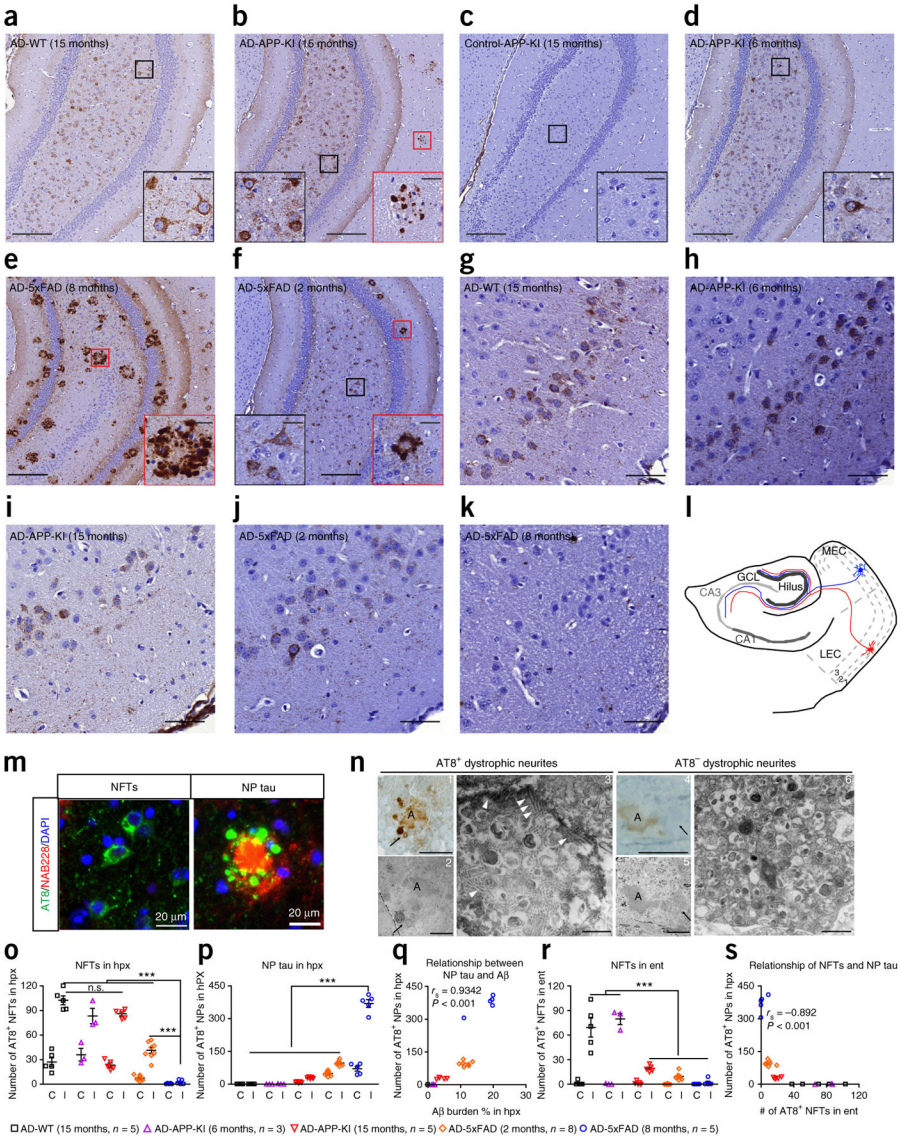

Figure 1.

Aβ plaques facilitate AD-tau induction of NP tau, rather than NFTs, at early seeding stages. (**a**–**f**) Representative immunostaining of pathological tau using the antibody AT8 in the ipsilateral ventral hippocampus dentate gyrus regions of 15-month-old WT ($n = 5$) (**a**), 15-month-old APP-KI ($n = 5$) (**b**), 6-month-old APP-KI ($n = 3$) (**d**), 8-month-old 5xFAD ($n = 5$) (**e**) and 2-month-old 5xFAD ($n = 8$) (**f**) mice at 3 m.p.i. with AD-tau and of 15-month-old APP-KI mice at 6 m.p.i. with age-matched control human brain lysate ($n = 3$) (**c**). Scale bars, 200 µm. Insets show a higher magnification of the corresponding areas in red (NP tau) and black (NFTs) boxes. Inset scale bar, 25 µm. (**g**–**k**) Immunostaining of the ipsilateral entorhinal cortex with AT8 for the mice used in **a**, **b** and **d**–**f**. Scale bar, 50 µm. (**l**) Schematic showing the perforant pathway and illustrating how Aβ plaques facilitate aggregation of tau as NP tau in the dystrophic axons of the hippocampus in the area where AD-tau is injected. This leads to fewer pathological tau seeds available to induce formation of NFT aggregates

in the connected somas located in entorhinal cortex. GCL, granule cell layer; MEC, medial entorhinal cortex; LEC, lateral entorhinal cortex. The number indicates the cortical layers, and red and blue cells depict two representative neurons. (**m**) Double labeling of Aβ (red) and tau (green) pathologies with NAB228 and AT8 monoclonal antibodies, respectively, in APP-KI (15 months) mice at 3 m.p.i. with AD-tau. DAPI (blue) stains nucleus. Scale bar, 20 μm. (**n**) Immunoelectron microscopy images of $AT8^+$ (images 1–3) and $AT8^-$ (images 4–6) dystrophic neurites around Aβ plaques. Images 1 and 4 are bright-field microscopy images, images 2 and 5 are corresponding low magnifications and images 3 and 6 are corresponding high magnifications. White arrowheads indicate examples of the fibrillar tau pathologies, and black arrows indicate the same dystrophic neurite throughout images 1–3 or 4–6. The letter A marks Aβ plaques. Scale bars in images 1 and 4, 25 μm; images 2 and 5, 10 μm; images 3 and 6, 500 nm. (**o**,**p**,**r**) The $AT8^+$ NFTs (**o**) and NP tau (**p**) in the hippocampus (hpx) and the NFTs in the entorhinal cortex (ent) (**r**) of the AD-tau-injected mouse cohorts represented in **a**–**k** were systematically quantified on both the ipsilateral (I) and contralateral (C) sides. One-way ANOVA with Tukey's multiple-comparisons test was performed; $^{**}P < 0.01$, $^{***}P < 0.001$; n.s., nonsignificant. (**q**,**s**) Positive correlation between Aβ burden and the induction of NP tau (Spearman correlation; $r_s = 0.9342$, $P < 0.001$) (**q**) and inverse correlation between NP tau in the ipsilateral hippocampus and NFTs in the ipsilateral entorhinal cortex (Spearman correlation; $r_s = -0.892$, $P < 0.001$) (**s**) for the mice represented in **a**–**f**. Data are presented as mean ± s.e.m. in **o**, **p** and **r**. The total protein amounts in AD and control brain lysates injected into each mouse were similar.

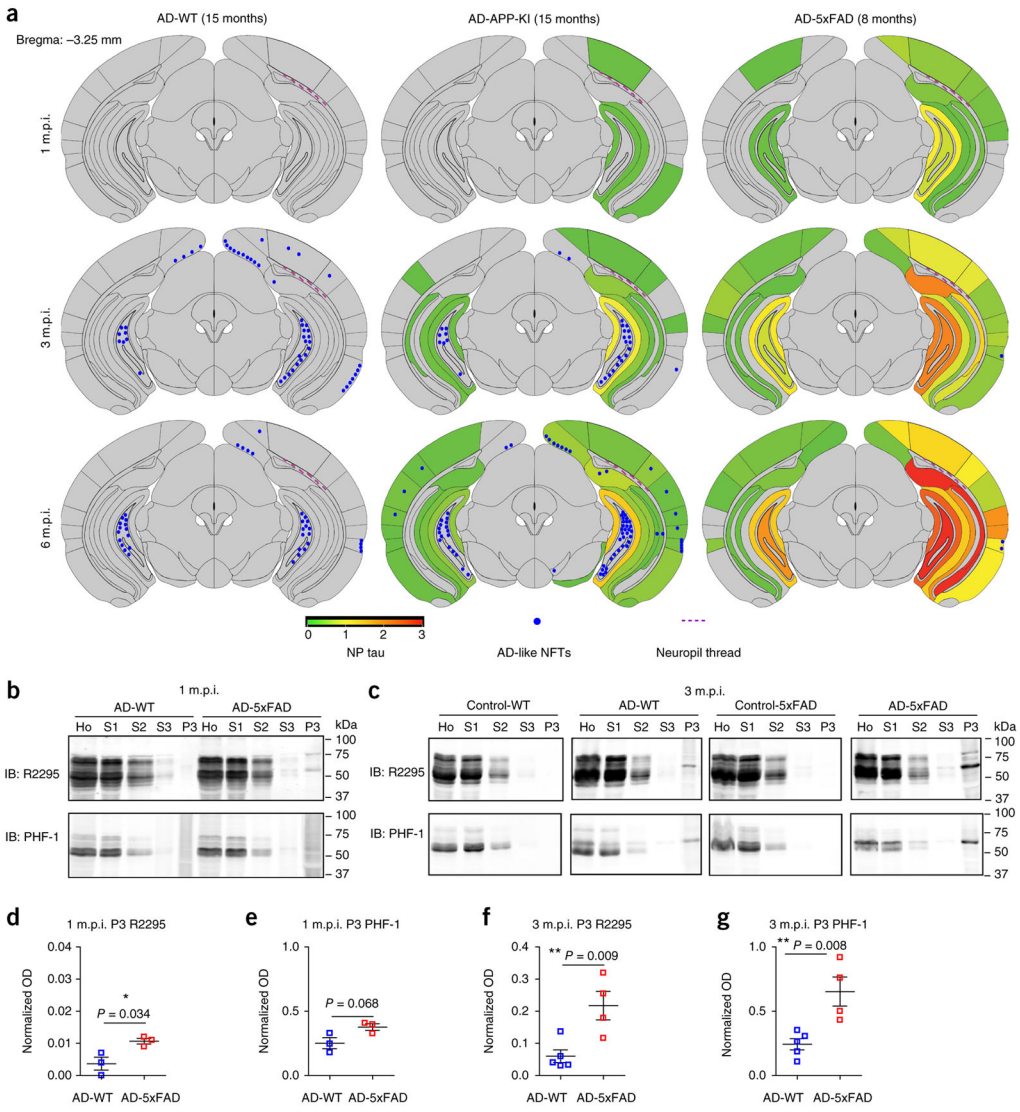

Figure 2.

NP tau aggregates faster and spreads more widely than NFT tau. (**a**) Semiquantitative analysis of AD-like NFT and NP tau pathologies based on AT8 immunostaining of brains from AD-WT (15 months), AD-APP-KI (15 months) and AD-5xFAD (8 months) mice at 1, 3 and 6 m.p.i. Representative coronal planes containing the ventral hippocampus are shown for each cohort, and seven additional coronal planes at 0.98, −0.22, −1.22, −2.18, −2.92, −4.48 and −5.52 with respect to bregma (coordinates in mm) are shown in Supplementary Figure 5a. Heat map colors represent the extent of NP tau pathology (gray (0), no pathology; red (3), maximum pathology). Average scores from each cohort of mice are presented. (**b**,**c**) Immunoblots after sequential extractions of hippocampus from WT and 5xFAD (8 months) mice with AD-tau or control injection at 1 m.p.i. (**b**) and 3 m.p.i. (**c**). Equal proportions of Ho, homogenate; S1, high-salt supernatant; S2, 1% Triton X-100 supernatant; S3, 1% sarkosyl supernatant; P3, 20-fold enrichment of 1% sarkosyl pellet relative to Ho were analyzed. (**d**,**e**) Quantification of P3 fractions immunoblotted with R2295 antibody selective

for mouse tau (**d**) and PHF-1 antibody for hyperphosphorylated tau (**e**) at 1 m.p.i. as shown in **b**. Three pairs of mice were quantified. (**f**,**g**) Quantification of the P3 fractions immunoblotted with R2295 (**f**) and PHF-1 (**g**) at 3 m.p.i. as shown in **c**. Five AD-WT and four AD-5xFAD mice were quantified. Optical density (OD) was normalized to that for the homogenate fraction from each corresponding mouse. A two-tailed *t*-test was performed; $*P \leq 0.05$, $**P \leq 0.01$. Data are presented as mean ± s.e.m. in **d**–**g**.

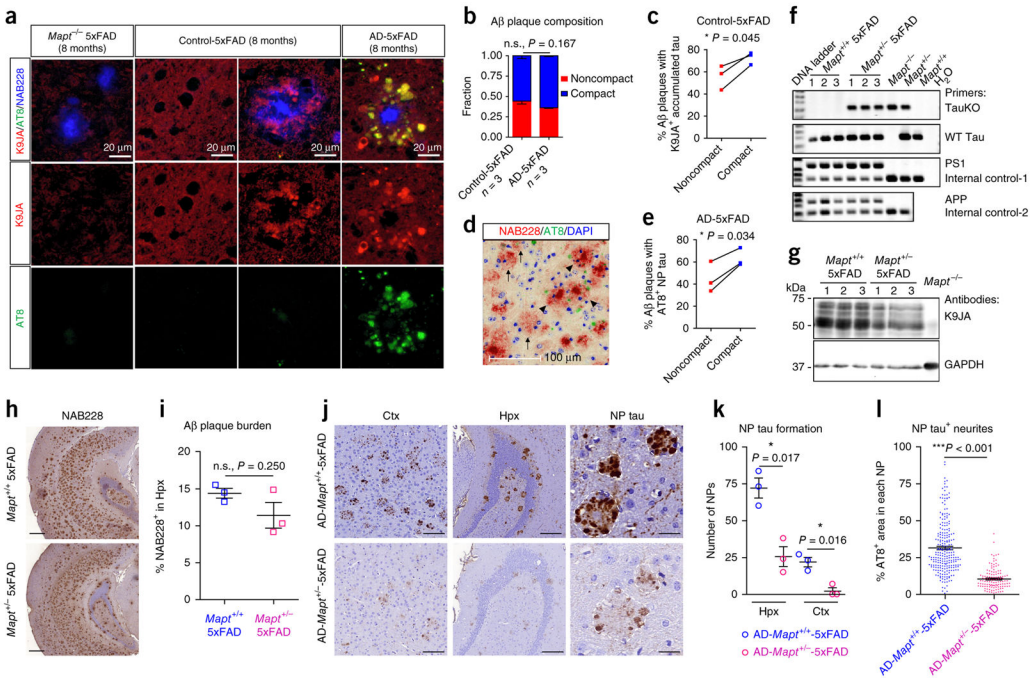

Figure 3.

Mislocalized tau in periplaque dystrophic axons is critical for AD-tau-induced NP tau aggregation. (**a**) Representative images of endogenous tau (red) detected by antibody K9JA in regions with or without Aβ plaques (blue) from 5xFAD mice with no endogenous tau ((*Mapt*$^{-/-}$ 5xFAD) (8 months)) or 5xFAD mice (8 months) injected with human control brain lysate or AD-tau at 3 m.p.i. Pathological tau (green) was detected by antibody AT8. Results from one out of three mice per group are shown. (**b**) Similar amounts of noncompact and compact plaques were present in control-5xFAD mice, and this ratio was not significantly altered in AD-5xFAD mice. (**c**) Proportion of each type of Aβ plaque surrounded by K9JA-labeled endogenous tau in control-5xFAD mice. Three mice were quantified. (**d**,**e**) Representative image (**d**) and proportion of each type (**e**) of Aβ plaque (red) surrounded by induced AT8-labeled NP tau (green) in AD-5xFAD mice. DAPI (blue) stains nucleus. In **d**, arrows indicate noncompact plaques and arrowheads indicate compact plaques. Scale bar in **d**, 100 μm. Quantifications in **b**, **c** and **e** were performed from the ipsilateral caudal hippocampal region of 5xFAD (8 months) mice injected with AD-tau or control at 3 m.p.i.; three mice per group were quantified. (**f**–**i**) Characterization of *Mapt*$^{+/-}$ 5xFAD mice ($n = 3$ per group). (**f**) PCR of genomic DNA confirming the genotype of *Mapt*$^{+/-}$ 5xFAD mice. The primers used for genotyping are indicated on the right. (**g**) Western blotting showing that endogenous mouse tau is reduced in *Mapt*$^{+/-}$ 5xFAD mice as compared to *Mapt*$^{+/+}$ 5xFAD mice. (**h**) Representative NAB228 immunostaining; scale bar, 400 μm. (**i**) Quantification of brain slices containing caudal hippocampus showing the Aβ plaque burden in 8-month-old 5xFAD mice with or without tau reduction. Two-tailed *t*-tests were performed; $*P \leq 0.05$. (**j**,**k**) Representative AT8 immunostaining (**j**) and quantification (**k**) of NP tau in both retrosplenial cortex (ctx) and hippocampus on the ipsilateral side of AD-tau-injected 8-month-old *Mapt*$^{+/+}$ 5xFAD and *Mapt*$^{+/-}$ 5xFAD mice at 1 m.p.i. ($n = 3$ per group). A dashed circle in **j** indicates a single NP. Scale bars in **j**: retrosplenial cortex,

100 μm; hippocampus, 200 μm; NP tau, 25 μm. (**l**) Quantification of NP-tau-positive neurites as a percentage of AT8 staining within each NP, as represented in the right panels in **j**. Over 100 NP tau from three mice per group were examined. A two-tailed *t*-test was performed; $*P \leq 0.05$, $***P \leq 0.001$. Data are presented as mean ± s.e.m. in **b**, **i**, **k** and **l**.

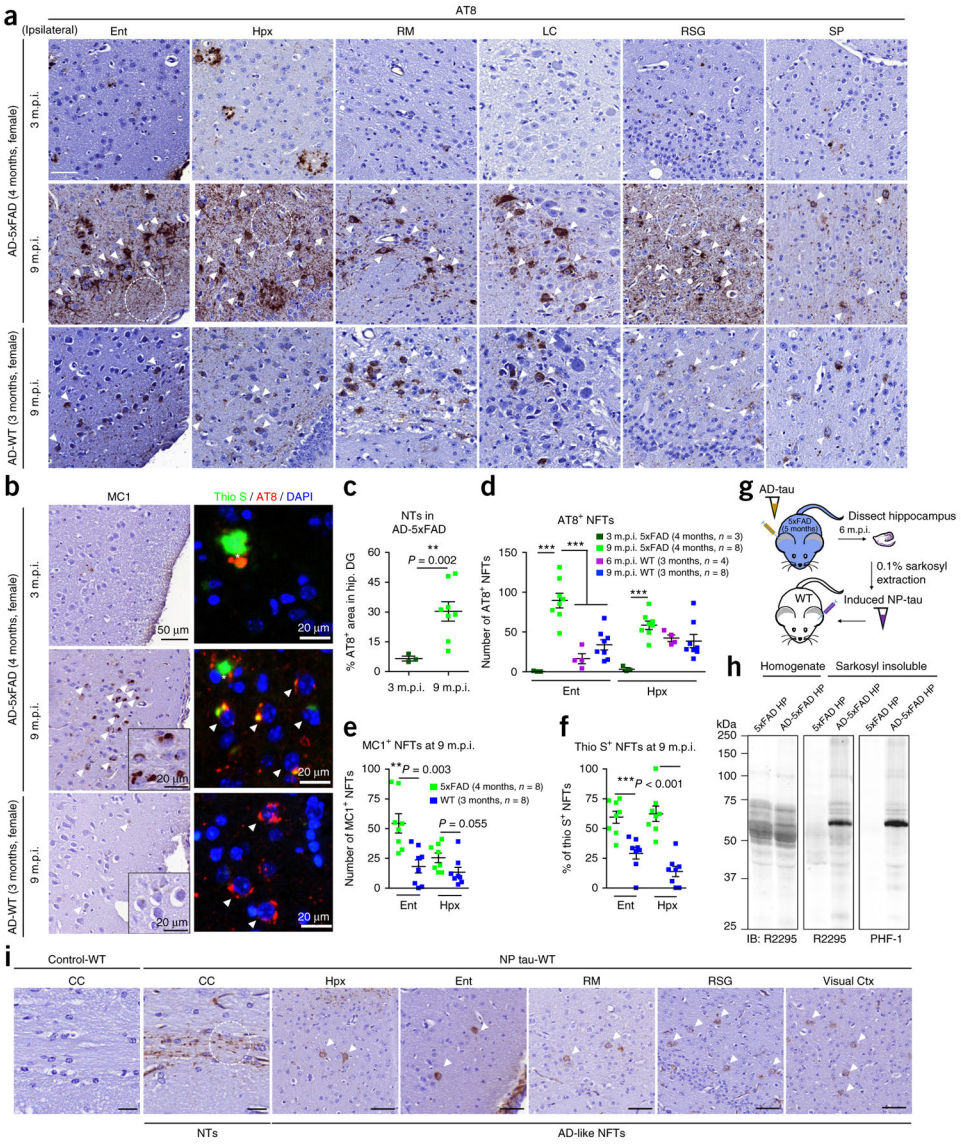

Figure 4.

NP tau triggers the formation of NFTs and NTs through secondary seeding events at later seeding stages. (**a**) Representative images showing tau pathologies as revealed by AT8 labeling in different brain regions on the ipsilateral sides of female AD-5xFAD (4 months) and AD-WT (3 months) mice from 3 to 9 m.p.i. of AD-tau. Three mice were analyzed at 3 m.p.i. and eight mice were analyzed at 9 m.p.i. Scale bar, 50 μm. RM, retromammillary nucleus; LC, locus coeruleus; RSG, retrosplenial granular cortex; SP, septal nucleus. (**b**) Representative images showing NFTs in AD-5xFAD (4 months) and AD-WT (3 months) mice detected by MC1 and thioflavin S (thio S). Thioflavin S–labeled β-sheet protein structure is stained in green, AT8-labelled pathological tau is stained in red and DAPI-labeled cell nucleus is stained in blue. Inserts are images with higher magnification. In **a**, **b** and **i**, white arrowheads indicate NFTs, white circles indicate NTs and asterisks indicate NP tau. (**c**) Quantification of AT8-labeled NTs as a percentage of the area occupied in the

hippocampal dentate gyrus (DG) region from AD-5xFAD (4 months) mice at 3 and 9 m.p.i., showing abundant NTs in AD-tau-injected 5xFAD mice at later time points. (**d**,**e**) Quantification of AT8-labeled (**d**) and MC1-labeled (**e**) NFTs in entorhinal cortex and hippocampus from the AD-WT and AD-5xFAD mice shown in **a** and **b**. (**f**) The maturation of AD-like NFTs was determined by the percentage of AT8-labeled AD-like NFTs with thioflavin S co-labeling at 9 m.p.i. in AD-5xFAD (4 months) and AD-WT (3 months) mice. The quantification results shown in **c**–**f** were from ipsilateral regions. A two-tailed *t*-test was performed; $*P \leq 0.05$, $**P \leq 0.01$. The size of each group in **a**–**f** is indicated in **d**. (**g**) Hippocampal tissues from AD-5xFAD (5 months) mice at 6 m.p.i. were extracted to obtain NP tau, which was reinjected into the hippocampus of WT mice to test its ability to induce NFTs and NTs *in vivo*. (**h**) Immunoblot showing that the induced pathological mouse tau in NP tau is present in the 0.1% sarkosyl–insoluble fraction. Equal proportions of Ho and 20-fold enrichment of 0.1% sarkosyl pellet relative to homogenate were analyzed with mouse-tau-specific antibody R2295 and hyperphosphorylated-tau-specific antibody PHF-1. Control lysates were extracted in the same way from the hippocampi of noninjected age-matched 5xFAD mice. (**i**) Representative images from three mice per group showing that AT8-labeled NTs and NFTs are present in multiple brain regions of WT mice injected with NP tau but are absent from those injected with control lysates at 3 m.p.i. Similar amounts of total protein in control and NP tau lysates were injected into each mouse. CC, corpus callosum. Scale bars in CC, 20 μm; in all others, 50μm. Data are presented as mean ± s.e.m. in **c**–**f**.

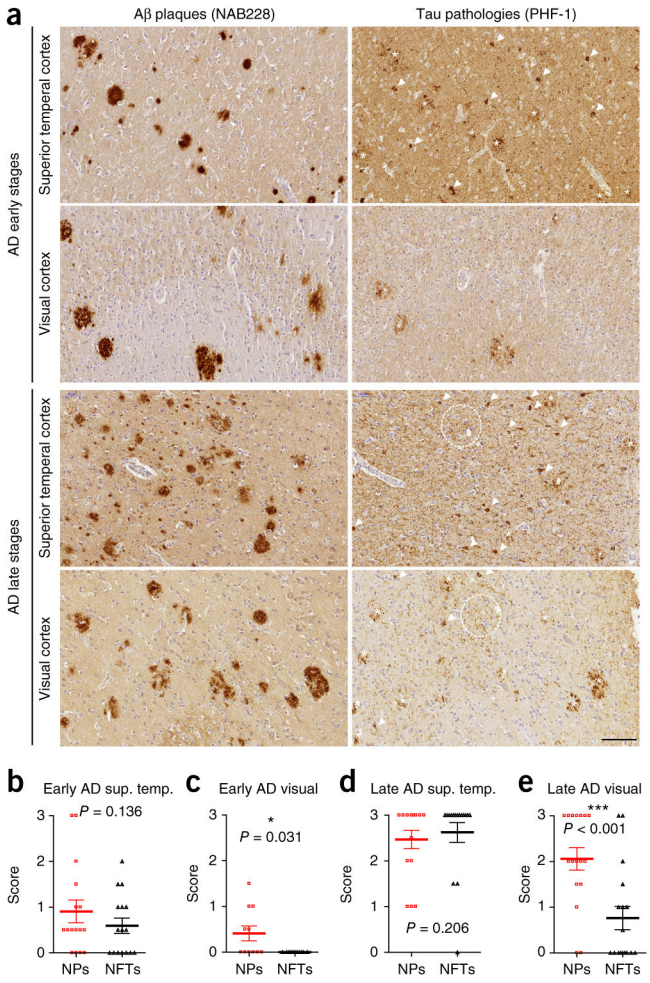

Figure 5.

NP tau appears earlier than NFTs in human AD brain. (**a**) Representative immunostaining with PHF-1 and NAB228 antibodies in superior temporal cortex and visual cortex on adjacent brain sections of one individual with AD from a set of 16 cases with early stages of AD pathology and of one individual with AD from a set of 17 cases with late stages of AD pathology, as determined using the most recent National Institute on Aging–Alzheimer's Association (NIA-AA) guidelines for the neuropathological staging of AD plaque and tangle pathology[24,34]. White arrowheads indicate NFTs, dashed white circles indicate NTs and the asterisks indicate NP tau. Scale bar, 100 μm. (**b**–**e**) A semiquantitative analysis of the pathologies of NP tau and NFTs in superior temporal cortex (sup. temp.) at early (**b**) and late (**d**) AD stages as well as in visual cortex (visual) at early (**c**) and late (**e**) AD stages. A two-tailed paired *t*-test was performed; $*P \leq 0.05$, $***P \leq 0.001$. Data are presented as mean ± s.e.m. in **b**–**e**.

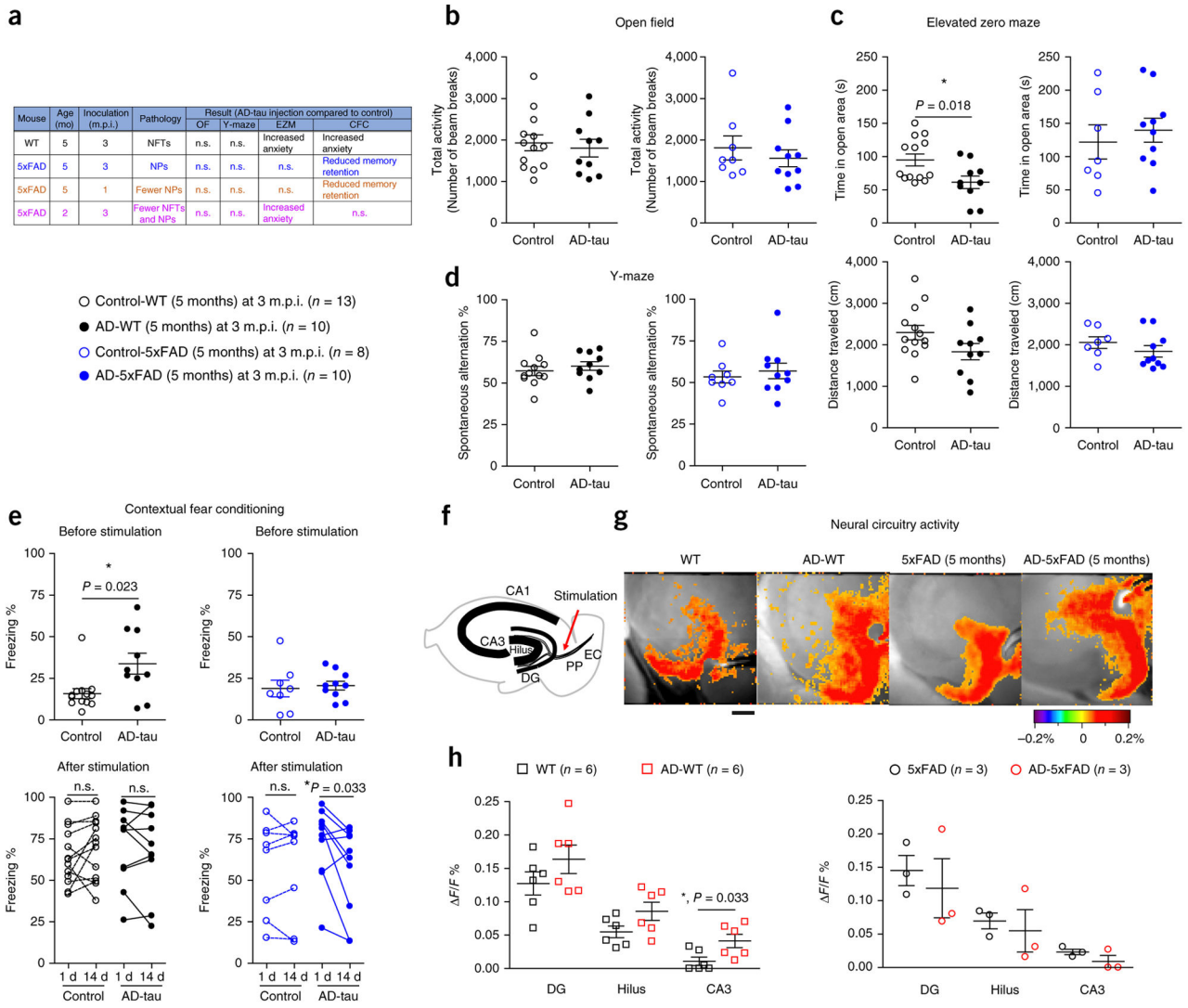

Figure 6.

The induced tau pathologies elicit effects on neural circuit activity and mouse behaviors. Mice with exclusively NFTs (AD-WT (5 months)) and exclusively NP tau (AD-5xFAD (5 months)) were tested for both behavioral and neural circuitry changes after 3 m.p.i. of AD-tau. (**a**) Brief summary of the behavioral results from all cohorts of mice presented here and in Supplementary Figure 9. OF, open field; EZM, elevated Z-maze; CFC, contextual fear conditioning. (**b**) Open field test showing no locomotor deficit in any of the mice. (**c**) Elevated zero maze results showing an anxiety-like behavior deficit in AD-WT (5 months) mice. (**d**) Spontaneous alteration behavior in the Y-maze reflecting short-term memory of the tested mice. Two-tailed *t*-tests were performed in **b**–**d**; $*P \leq 0.05$, $**P \leq 0.01$. (**e**) Contextual fear conditioning was performed to assess the basal anxiety level and long-term memory of the mice. The percentage of time each mouse exhibited freezing behavior during the test period was recorded as 'Freezing %'. The response changes for each individual mouse from 1 to 14 d post-stimulation reflect the remote memory retention of the tested mice. Two-way ANOVA with time as a repeated measure was performed; AD-5xFAD (5

months): time ($P = 0.047$, $F = 4.649$, degrees of freedom (DF) = 1), AD-tau treatment ($P = 0.618$, $F = 0.259$, DF = 1) and interaction ($P = 0.061$, $F = 4.054$, DF = 1). This was followed by a two-tailed paired *t*-test. Each group contained 8–13 mice, and each mouse is indicated as a dot in the graphs. (**f**) Diagram showing the hippocampal regions in which voltage-sensitive dye fluorescence was recorded on the brain slices. PP, perforant pathway; EC, entorhinal cortex. (**g**) Representative pseudocolored images of neural activity recorded from WT ($n = 6$), AD-WT ($n = 6$), 5xFAD ($n = 3$) and AD-5xFAD ($n = 3$) mice depicting the change in membrane potential measured as the relative time-resolved fluorescence of a voltage-sensitive dye loaded into hippocampal slices prepared from WT and 5xFAD mice with or without AD-tau injection. Scale bar, 300 μm. (**h**) Quantification of the membrane potential changes in sequential hippocampal regions activated by stimulation of the perforant pathway: dentate gyrus, hilus and area CA3 in the mice injected with AD-tau or control. Data shown in the graphs are from 3–6 mice, as indicated. Data for two to three brain slices per mouse were recorded and averaged to produce a single value for each mouse. Two-way ANOVA with region as a repeated measure was performed; WT mice: region ($P < 0.0001$, $F = 29.93$, DF = 2), AD-tau treatment ($P = 0.0045$, $F = 11.17$, DF = 1) and interaction ($P = 0.9635$, $F = 0.03729$, DF = 2). This was followed by a *t*-test with Welch's correction; $^*P \leq 0.05$. Data are presented as mean ± s.e.m. in **b**–**e** and **h**.